

Differentiable Land Model Reveals Global Environmental Controls on Ecological Parameters

Jianing Fang¹, Kevin Bowman², Wenli Zhao¹, Xu Lian¹, and Pierre Gentine¹

Affiliations

1. Department of Earth and Environmental Engineering, Columbia University, New York, NY, USA
2. Jet Propulsion Laboratory, California Institute of Technology, Pasadena, CA, USA

Corresponding authors: Jianing Fang (jf3423@columbia.edu), Pierre Gentine (pg2328@columbia.edu)

Abstract

Accurate modeling of terrestrial carbon and water exchange requires robust ecological parameters that capture vegetation responses and adaptations to the local environment. The current generation of land models use Plant Functional Types (PFTs) to discretize vegetation functional diversity, but these coarse categorizations often overlook fine-scale variations shaped by local climate, soil, and forest age factors. The lack of governing equations for plant adaptation demands a paradigm shift in how we integrate diverse Earth observations to uncover ecological functional dependence on changing environments. To address this challenge, we developed DifferLand, a differentiable, hybrid physics and machine learning model that infers the spatial distributions of ecological parameters and their relationships with environmental factors constrained by satellite and in-situ observations. Our model unifies top-down and bottom-up observational constraints with process-based knowledge to generate a global analysis of ecological functions and their adaptation to environmental gradients. We found PFTs account for less than half of the explainable spatial parameter variations controlling carbon fluxes and vegetation states. The remaining parameter variability is largely driven by local climate and forest demography factors, and the learned environment-parameter relationships lead to enhanced spatial generalization at unseen locations. DifferLand identified growing season length, leaf economics, and agricultural intensity as the three orthogonal spatial gradients underlying parameter variations. Our novel framework can lead to new insights on global carbon cycling by learning directly from data and expanding our understanding of local responses of ecosystems to environmental drivers.

Key Words: differentiable modeling, hybrid modeling, adaptation, model-data fusion

The dynamic interplay between plant communities and environmental factors is influenced by fast and slow drivers, ranging from short-term physiological response to processes operating over evolutionary and geological time scales¹. The distribution of spatially-aggregated plant functional traits represents a snapshot of dynamic plant strategies and community compositions, shaped by both long-term natural selection^{2,3} and recent disturbance history⁴. Terrestrial biosphere models (TBMs) often prioritize explicitly resolving the fast process dynamics (e.g., stomatal response to VPD, response of heterotrophic respiration) driven by external forcings but approximate slow-evolving processes as time-invariant parameters subsumed into empirical relationships (e.g. fixed turnover rates of slow carbon pools)⁵. The heterogeneity of the land surface, the nesting of processes across multiple temporal scales, the stochastic nature of plant-environment interactions, and more importantly, plant acclimation and adaptation to local climate create diverse ecological niches but also present significant challenges in ecological functions across the diverse and heterogeneous landscapes under a changing climate⁶.

TBMs require robust spatialization strategies to approximate the functional diversity of different ecosystems. To characterize the diversity of plant types, the current generation of models categorize a group of plant functional types (PFTs) based on their life form (e.g., deciduous versus evergreen forest, broadleaf versus needleleaf forest), prescribing a specific set of fixed ecological parameters for each physiognomy assemblage⁷. Functional diversity can be partially represented by co-occurring sub-grid PFTs tiles competing for resources such as light, water, and nutrients⁸. However, the conventional PFT categorization largely misses plant adaptation and acclimation to local environmental gradients shaped by prevailing climate, topography, disturbance⁸. Additionally, studies have shown that key physiological parameters such as leaf area, leaf nitrogen content^{9,10}, unstressed stomatal conductance¹¹, and hydraulic vulnerability¹² often exhibit spatial variations that do not align with the boundaries of predefined PFTs (plant functional types). Recent modeling efforts have proposed incorporating new dimensions of parameter variability, including ecological succession, hydrological regimes, soil texture, and soil fertility⁸. However, indiscriminately increasing parameter dimensions can quickly lead to the 'curse of dimensionality,' significantly complicating model complexity and amplifying parametric uncertainties⁸. Thus, a key challenge remains: how to better represent land surface heterogeneity while managing model complexity.

Trait-based modeling has recently emerged as a new paradigm for land modeling by replacing empirical PFT-based parameters with measurable, spatially explicit plant trait parameters¹³. However, running

global trait-based models require spatially contiguous maps of plant traits. Most of the needed plant traits (e.g., Q10, photosynthetic capacity, leaf mass per area, allocation fractions) cannot be directly retrieved by remote sensing techniques, and they are typically generated by “bottom-up” upscaling of site-level observations using empirical trait-environment relationships¹⁴ or “top-down” parameter inference through model-data fusion (MDF)^{9,12,15} that are likely to miss the complexity of those relationships. The logic behind empirical upscaling is that ecologically-viable plant traits represented by model parameters are determined by environmental conditions such as climate, soil, and canopy properties. Machine learning (ML) algorithms have been shown effective for capturing complex non-linear relationships between environmental predictors and spatial parameter patterns. Yet, it remains uncertain whether spatial upscaling of individual trait-based parameters offers better predictions of global carbon and water exchange compared to traditional PFT-based approaches.^{16,17} The main challenges of such empirical upscaling strategies include 1) the inherently weak relationships between individual traits and environmental predictors due to trait equifinality and phenotypic plasticity¹⁸; 2) multiple compensating errors and uncertainties in TBMs that obscure the effect of individual traits¹⁶; 3) the lack of physiological constraints in purely data-driven ML models and the uneven distribution of samples can lead to large biases in model training and validation¹⁹.

By contrast, the MDF approach constrains the (prior distribution of) ecological parameters within a process-based model by ecological observations to yield posterior distributions of ecological parameters that can be unobservables²⁰. When given appropriate observational constraints, model-data fusion can provide physically-consistent estimates of ecological parameters and account for covariance relationships between parameters reflecting trait coordination or tradeoff¹². However, global observations needed to constrain the relevant parameters are often available only at point level (e.g., eddy-covariance sites, forest plots, and soil profiles) or coarse spatial grids (e.g., atmospheric inversions and satellite gravimetry based terrestrial water storage) and the computational cost of running a globally constrained model can be unachievable. Thus, the resulting parameters independently retrieved at different locations or at different pixels still need to be interpolated or downscaled to generate usable global maps^{21,22}. Furthermore, independent assimilation across sites neglects useful information of spatial correlations information between ecological parameters, which should be leveraged to reduce equifinality and generate robust spatial patterns of ecological parameters.

Unifying Top-Down and Bottom-Up Constraints of Ecosystems Functions Through Hybrid-ML Modeling

In this study, we unify the flexibility of machine learning with the observational consistency of model-data fusion (MDF) through a novel terrestrial differentiable framework called DifferLand, a hybrid-ML framework enabling spatializing ecological parameters (Fig. 1). Our approach is based on the idea that trait-based parameters function as latent variables within ecosystems, collectively mediating the relationship between long-term environmental conditions and dynamic ecological variables driven by short-term fluctuations. Rather than inverting model parameters independently at different grid cells (as in most MDF studies) or estimating the each variable separately from empirical relationship (as in most ML-based upscaling), we couple a global spatialization neural network (NN) (Fig. S1) with an intermediate-complexity TBM that predicts photosynthesis, carbon allocation, turnover, the water cycle, and fire disturbances across different grid cells (Fig. S1-S2), which is constrained end-to-end by global observations. This hierarchical design allows the parameter-environment relationship to be retrieved from data, efficiently integrating the mechanistic constraints of the TBM (e.g., conservation of mass over time). Importantly, this framework enables learning the spatial dependence of trait coordination arising from plant adaptation and acclimation to local environmental conditions. We train the hybrid model on seven remote-sensing informed datasets, three eddy-covariance flux variables, and a global soil carbon estimate (Fig. S2), effectively incorporating both bottom-up and top-down constraints into the retrieved parameter patterns. Uncertainties associated with model initialization, non-convex optimization, and parameter equifinalities are further analyzed by training an ensemble of randomly initialized models with bootstrapped data sampling to evaluate the robustness of the learned environment-parameter relationships (see Methods for details).

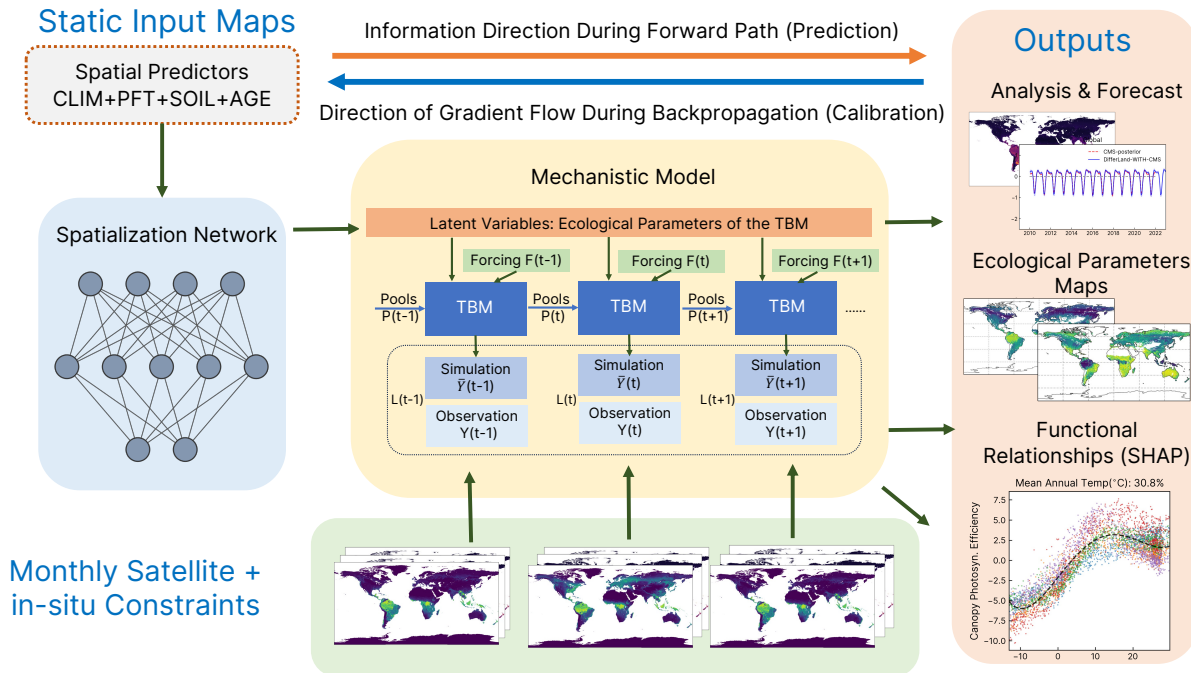


Fig. 1 | Schematics of the DifferLand framework. The model consists of a spatialization neural network that takes as input 10 PFT classes, three climatology and elevation variables (CLIM), two forest age and maximum canopy height variables (AGE), and five soil texture variables (SOIL) to predict the 40 ecological parameters (including initial conditions of water and carbon pools) within an intermediate-complexity terrestrial biosphere model. During the forward pass, the spatialization neural network takes a batch of spatial predictors to estimate all model parameters and initial conditions for the TBM, which is then integrated forward with forcing variables to generate decadal time series of ecological variables (orange arrow). During the backward pass, the gradient of the loss function—calculated between the modeled and observed time series (green box) across all pixels—is backpropagated through the entire TBM via automatic differentiation to calibrate the spatialization neural network (blue arrow). The calibrated model can output analysis and forecast of the state and fluxes of the terrestrial carbon and water cycle and provide global estimates of ecological parameters. The learned functional relationships between spatial predictors and each model variable can be investigated from the calibrated NN using explainable AI (artificial intelligence) techniques to yield new insights on local adaptation.

DifferLand effectively captures the spatial-temporal patterns of in-situ and remotely-sensed observations of vegetation dynamics from 2010-2023 (Fig. S4-S5). Importantly, the model demonstrates minor differences in predictive performance between the training and test pixels (see Fig. S3), suggesting the model generalized well at unseen pixels (Fig. S4-S5). When trained on a full set of 20 predictors (PFT+CLIM+SOIL+AGE), the ensemble of models (N=20) accurately simulates satellite-based monthly leaf

area index (LAI), solar-induced fluorescence (SIF), vegetation optical depth (VOD), and estimated evapotranspiration (ET) at 0.25° resolution over held-out pixels with an overall R^2 (ensemble mean \pm SD) of 0.90 ± 0.01 , 0.81 ± 0.01 , 0.86 ± 0.01 , 0.66 ± 0.01 , and predicted the annual live biomass with an R^2 of 0.88 ± 0.01 (Fig. S4-5). The temporal correlations (r) between observed and predicted LAI and SIF exceed 0.8 across most temperate and boreal biomes, though they are slightly lower in tropical forests and Australia. This is partly due to model limitations in representing the interactive processes (e.g., water-light tradeoffs and nutrient limitations) that control vegetation phenology in tropical forests, and large observation uncertainties and low signal-to-noise ratio in both regions.²³⁻²⁵ (Fig. S6a-b). The model also predicts CMS-Flux net biosphere exchange (NBE) and GRACE gravimetry-based equivalent water thickness (EWT) anomalies at 4°x5° (due to coarser resolution of the constraints) with R^2 of 0.79 ± 0.01 and 0.58 ± 0.01 , respectively.

In addition, we evaluated the model prediction of gross primary productivity (GPP), ET, and ecosystem respiration (RECO) against 187 eddy covariance sites with more than 12 months of observations that overlap with the simulation (Fig. S9). We found the model achieved good agreement with site-level fluxes in mean spatial gradients, achieving spatial correlation of 0.88 for GPP, 0.84 for RECO, and 0.71 for ET (spatial correlation of 0.85, 0.82, and 0.72 on held-out sites, Fig. S11). Furthermore, the model also captured temporal variations in GPP, ET, and RECO, despite the spatial mismatch between model pixels at tower footprints (Fig. S10 & S12). Globally, the model ensemble simulates a net land carbon sink of -2.50 ± 0.59 PgC/year, which is within the range of CMS-Flux's estimates of -2.08 ± 0.10 PgC/year over vegetated land surfaces (Fig. S7). The model simulates Northern Hemisphere temperate and boreal regions as strong terrestrial carbon sinks, and Australia, Tropical Asia, South America, and Africa as near neutral, consistent with the satellite-constrained NBE inversions assimilated into the model (Fig. S7-8).

Parameter Spatialization Reveals Regional Diversity in Environmental

Predictability of Ecological Functional Parameters

DifferLand's ability to simulate ecological states and fluxes derives from the joint constraint contributions from model physics and data assimilation globally retrieved parameters. To assess the extent to which environmental predictors (i.e., adaptation to local environmental gradients) offer additional predictive power to simple PFTs, we conducted a full factorial experiment by including or excluding each group of the PFT, CLIM, AGE, SOIL predictors and assessing their impact on the global predictions. We then used a

hierarchical partition algorithm²⁶ to isolate the independent contributions of different predictor groups. We estimated from a control experiment where a white noise variable replaced the spatial predictors. The white noise variable contains no spatial information and serves as a baseline for model performance without considering parameter spatialization. After hierarchical partition, the sum of explained variance from this control case and that assigned to each of the predictor groups equals the performance of the model using the full set of predictions, emphasizing that the partition method was sound (Fig. 2).

We find spatialization of ecosystem parameters explains around 10-56% of the total spatiotemporal variance in predicted ecological variables (Fig. 4f), particularly for carbon-cycle related variables including NEE (56%), LAI (37%), SIF (29%). However, variabilities in water-cycle related variables such as EWT and ET are mostly controlled by model structure and forcing (81% and 90%, respectively). In other words, plants can locally adapt to adjust carbon cycling but their adaptation only marginally affects the local water cycle. Among the spatial predictors, PFTs contributed to less than half (24-36%) of the total variance explained by spatial parameter variability, demonstrating the limit of this approach and the need to go beyond a PFT-split of the world in land-surface modeling. Although PFTs contributed the most to the total explained variance for LAI (16%), CLIM variables have the most prominent role in the prediction of NEE (20%) and EWT (7%). For SIF, PFT and CLIM variables have around equal share in the explained variance. AGE and SOIL predictors are important for NEE that integrates carbon stock and respiration signals, explaining 13% and 7% of the total variability, emphasizing the key role of forest age and soil on terrestrial carbon uptake.

Next, we partitioned the temporal signals at each pixel to identify locations where each spatial predictor group explained the largest variabilities. For LAI (Fig. 2a), NBE (Fig. 2b), SIF (Fig. 2c), and ET (Fig. 2e), we found model structure and forcing explain the majority of the variance in boreal and temperate regions. In contrast, parameter spatialization played a more significant role in simulating carbon and water dynamics within tropical and subtropical ecosystems, which are characterized by less pronounced seasonal variations in temperature and radiation, yet exhibit a higher degree of ecological diversity. PFT fractions explain the largest variance in tropical broadleaf forests and areas with sharp ecotones or steep land-use intensity gradients caused by deforestation and cropland expansions, such as at the periphery of Amazon basin and the Himalayan foothills. CLIM variables have larger roles in mid- to high- latitude regions and biomes with annual plants (e.g., grasslands), whereas AGE variables (i.e., estimated forest age and canopy height) influence carbon fluxes over perennial vegetation and are important for

differentiating vegetation states within forest biomes. For EWT (Fig. 2d), model structure and forcings explain the greatest variance in tropical, monsoonal, and semi-arid regions, where water availability varies significantly. In boreal and energy-limited regions, effects from PFT and CLIM predictors become important. Overall, these findings suggest that parameter spatialization has a larger impact in regions with high spatial heterogeneity but milder seasonal cycles, while forcing variables explain most of the variance in areas dominated by temporal variabilities.

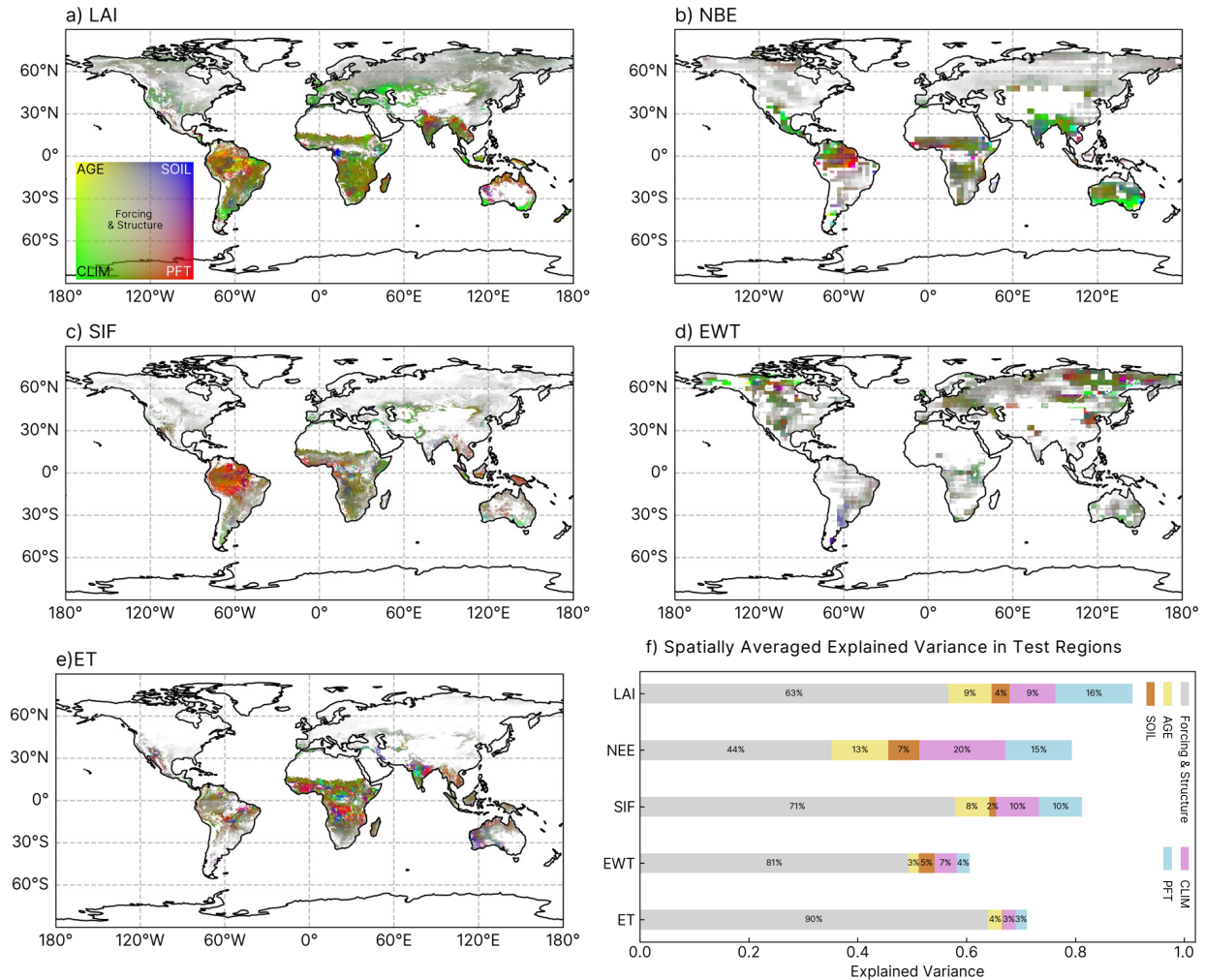


Fig. 2 | Hierarchical partitioning of explained variance by four predictor groups in addition to model structure and forcing. Panels a-e illustrate the proportion of explained variance from the five components along temporal dimensions across space for LAI, NEE, SIF, EWT, and ET respectively. The color gradient in the inset of panel a indicates the dominant predictor group for model parameter spatialization in simulating the observed variable, while color saturation reflects the relative importance of meteorological forcings and model structure versus parameter spatialization in capturing the temporal correlations of the variable. Panel f presents the partitioning of

explained variance across both space and time, aggregated over test pixels for LAI, NEE, SIF, EWT, and VOD. The percentage contribution of each component to the total explained variance is labeled in the plot. For further results on the relative contribution of predictor groups, see Fig. S17.

We then examine the spatial patterns of the model-estimated ecological parameters. Given that our model includes 40 parameters with varying sensitivities to the assimilated datasets, we conducted a parameter identifiability analysis to select parameters exhibiting robust patterns across independently initialized ensemble members. (Fig. S19 & S20). We find that parameters controlling ecological processes on seasonal or shorter time scales, such as phenology (the timing of leaf onset and senescence), leaf carbon mass per area (LCMA), canopy photosynthetic efficiency, and evapotranspiration ($uWUE$ and r_b) can be robustly constrained by the assimilated datasets. Additionally, the model ensembles learn consistent patterns of carbon use efficiency (CUE), the allocation fractions to labile, root, and wood pools, the sensitivity of heterotrophic respiration to temperature (Q10) and precipitation (θ_p), and the residence time (the inverse of turnover rate) of the labile (τ_{labile}), foliar (τ_{foliar}), and litter pools (τ_{litter}).

We compared the retrieved CUE, Q10, and LCMA values with independent datasets and site-level measurements. DifferLand learns a global mean CUE of 0.40 ± 0.03 with spatial variations from 0.23 to 0.78, agreeing well with a global synthesis of over 200 site-level studies with global mean at 0.46 and range 0.22-0.79²⁷. The retrieved CUE exhibits a decreasing latitudinal trend from boreal to tropical forest biomes (herbaceous biomass excluded due to uncertainties in observation constraints), consistent with the patterns from site measurements²⁷ and Moderate Resolution Imaging Spectroradiometer (MODIS) NPP/GPP products²⁸ (Fig. S23). The retrieved Q10 has a global mean of 1.78, with lower values in tropical forests (1.49) compared to other biomes. This is generally consistent with both the global mean value (1.72) and the spatial patterns of Q10 reported in a previous study using a different process-based terrestrial carbon model. (Fig. S24)²⁹. For LCMA, the model estimated high values in wet tropics and semi-arid regions, and low values in temperate deciduous and boreal forests agreeing with global maps statistically upscaled from trait databases^{9,30}, although the absolute values of peak LCMA are lower than estimates from statistical upscaling maps of plant traits, potentially due to the substantial scale differences between level-level measurements and the grid-scale resolutions (Fig. S25).

In contrast to the good performance of short-term processes, parameters related to processes on multiannual to multi-decadal timescales, such as wood turnover (τ_{wood}), litter to soil organic matter

decomposition rate (k_{decomp}) and SOM turnover (τ_{SOM}), are subject to larger uncertainties. The ensemble means and standard deviations of residence time and allocation fractions (Fig. S21-22) are broadly consistent with previous pixel-level model-data fusion studies at coarser resolution⁹, but exhibit smoother patterns with reduced local noise, due to the use of a global spatialization network and spatially continuous predictors.

Functional Form of Environment-Parameter Relationships Diagnosed from the Spatialization Network

To understand the dependence of the ecological parameters on climate, soil and age parameters, we applied SHAP explainable AI analysis (Methods) on the spatialization neural network. When both PFT classes and environmental variables are used, all PFT classes combined explain around 40-50% of the spatial variability as measured by absolute SHAP values (Fig. S26), consistent with the results from hierarchical partition (Fig. 2e). Considering that interactions between PFTs and environmental variables may confound our results (e.g., parameters differ by PFTs even in the mean values), we used models trained with only environmental variables to extract the functional form of environment-parameter relationships for six key ecological parameters: canopy photosynthetic efficiency, autotrophic respiration fraction, Q10, root allocation fraction, leaf lifespan, and LCMA (Fig. 3).

We found a predominant effect of mean annual temperature (MAT) on all six parameters (30-50%), indicating a first-order temperature regulation on global vegetation parameters (Fig. 3). Further, such temperature dependence is non-linear, with a positive increase up to 14°C and a decline at higher temperature (Fig. 3a). Similarly, autotrophic respiration fraction increases with MAT in cool conditions before reaching a plateau after around 10 °C (Fig. 3b). The saturation of temperature dependency is also observed for root allocation fraction, albeit in the reverse direction (Fig. 3d). Max canopy height—an integrated variable reflecting resource availability, hydraulic pressure, and disturbance history—was found important for predicting canopy photosynthetic efficiency (Fig. 3a), Q10 (Fig. 3c), root allocation fraction (Fig. 3d), and leaf carbon mass per area (Fig. 3f), all decline in taller-canopy vegetation. Tree age has a negative relationship on canopy photosynthetic efficiency up to 150 years, suggesting higher photosynthetic capacity in younger forests (Fig. 3a). Precipitation positively controls autotrophic respiration fraction, leaf lifespan, and leaf carbon mass per area, although the relationships are more subdued compared with temperature dependencies.

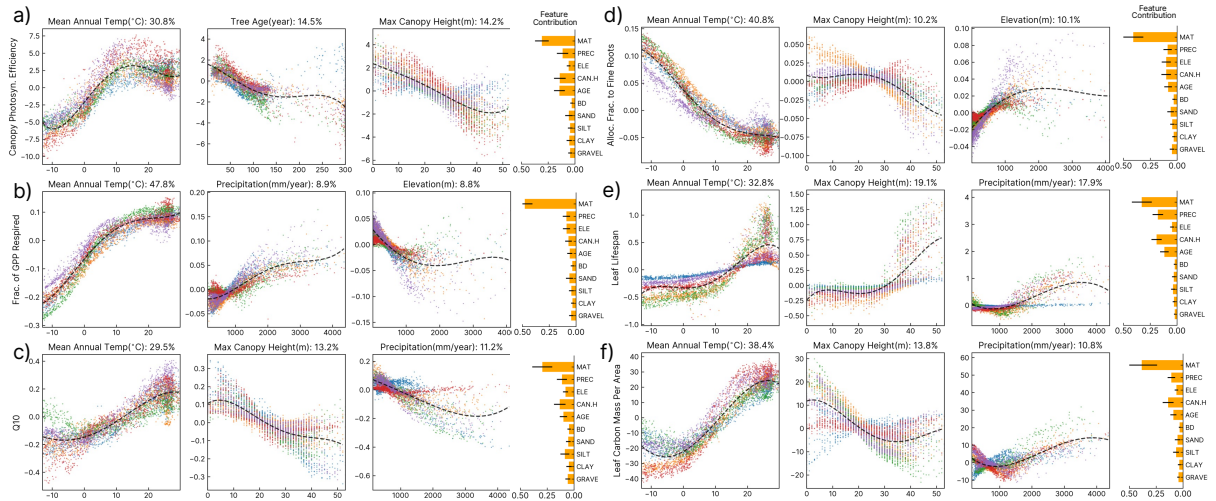


Fig. 3 | Environment-Parameter Relationships Captured by the Spatialization Network. Features are ranked by their ensemble-averaged absolute SHAP values. Different colors represent results from five independently calibrated DifferLand runs. 1000 randomly selected 0.25° pixels were sampled from each run. SHAP values for each model parameter are normalized using the minimum and maximum values from each run. A fourth-degree polynomial, fitted using ridge regression with a regularization coefficient of 0.5, shows the combined results from all five runs. The percentage above each subplot indicates the proportion of absolute SHAP values (i.e., explained power) of the considered feature relative to the sum of absolute SHAP values of all predictors. MAT: mean annual temperature; PREC: annual precipitation; ELE: elevation; CAN.H: max canopy height; AGE: tree age; BD: soil bulk density; SAND: soil sand fraction; SILT: soil silt fraction. CLAY: soil clay fraction; GRAVEL: soil gravel fraction.

Spatial Convergence of Ecological Parameters Reflects Plant Traits Coordination

To disentangle the main drivers of global variability in ecological parameters, we performed a principal component analysis (PCA) on 13 spatially robust and ecologically meaningful parameters to identify the primary drivers of their spatial variability. (Fig. 4). PC1 (Fig. 4b), explaining 50.2% of the variability, reflects global growing seasonal length and is positively correlated with live biomass density ($r=0.2$, $p<0.001$). LCMA, leaf lifespan, and leaf onset and falling durations (higher values in warm and wet environment) align with the positive PC1 direction, whereas fine roots allocation points to the reverse direction (more carbon to roots in cool and dry environment) (Fig. 4a). PC2 (Fig. 4c) accounts for 23.1% of the spatial variability and reflects leaf economics as it is correlated to both global leaf nitrogen content³⁰ ($r=0.57$, $p<0.001$) and the distribution C4 vegetation characterized by higher photosynthetic efficiency in semi-arid regions ($r=0.52$, $p<0.001$). Canopy photosynthetic efficiency, uWUE, and Q10 positively scale along PC2, whereas carbon allocations to labile and foliar pools orient in the opposing direction (Fig. 4a). PC3 (Fig. 4d) explains 10.0% of the spatial variability and reflects global cropland cover

($r=0.28$, $p<0.001$), characterized by high canopy photosynthetic efficiency and fast litter turnover, possibly due to fertilization and crop harvesting (Fig. 4a). Together, these three PCs explain 83.3% of the spatial variability among the 13 considered ecological parameters, highlighting strong plant trait coordination driven by growing season length, leaf economics, and agricultural intensity gradients. We further emphasize that those regions were not imposed but retrieved as the emergent behavior of the global model-data fusion.

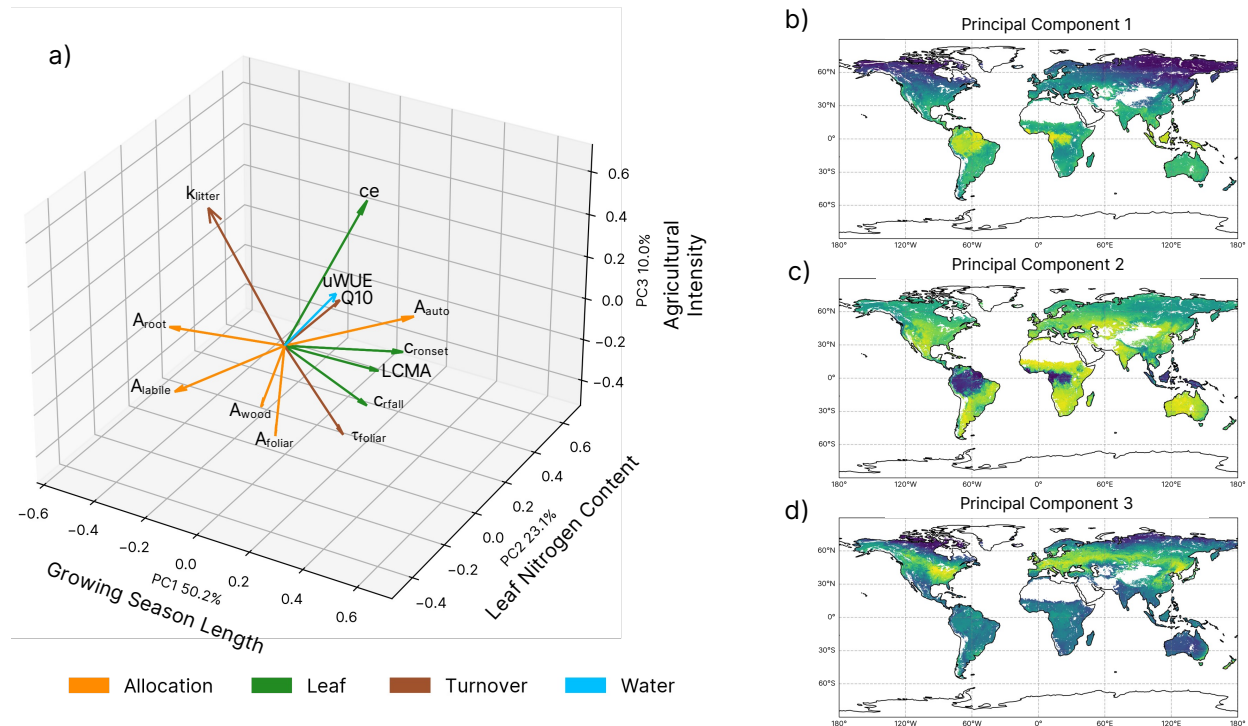


Fig. 4 | Principal component analysis (PCA) on the spatial variations of selected ecological parameters. These parameters are selected based on the model identifiability test (See Methods for details). a) illustrates the ordination of the 13 parameters within the space spanned by the first three principal components (PCs). Each PC's share of explained variance is labeled next to the axes. The 13 parameters include canopy photosynthetic efficiency (ce), underlying water use efficiency ($uWUE$), temperature sensitivity of heterotrophic respiration (Q_{10}), autotrophic respiration fraction (A_{auto}), leaf carbon mass per area ($LCMA$), leaf onset (c_{ronset}) and fall duration (c_{rfall}), leaf lifespan (τ_{foliar}), and allocation fraction of GPP to labile (A_{labile}), foliar (A_{foliar}), wood (A_{wood}), and fine roots (A_{root}) pools; b-d) plot the spatial maps of the top three PCs.

Discussions

DifferLand demonstrates a scalable method for retrieving the dependencies of global ecological parameters to climate, age and soil. Constrained by both in-situ and remote sensing data, DifferLand enables robust spatial predictions of vegetation dynamics, including carbon and water fluxes, even at previously unobserved locations due to the high generalizability of the hybrid model. The model can be trained efficiently and globally in about five to eight hours on two CPU cores with automatic differentiation. We found all climatology, forest age, max canopy height, and soil properties predictors combined captured comparable or even larger proportions of the spatial variabilities in model parameters compared with PFTs (Fig. S26). Crucially, we showed that including environment-parameter relationships lead to a marked improvement in the simulation of global ecosystem carbon cycling, particularly at capturing ecological gradients within regions defined by the same PFTs.

We note that the conclusions drawn from this research are dependent on the timeframe considered for the observations. In this 14-year study, spatial predictors were treated as temporally invariant, under the assumption that their temporal variations are negligible compared to their mean spatial gradients. Furthermore, we assumed that the relationships between parameters and the environment remained stable throughout the study period, implying that plant acclimation and adaptation to environmental changes occur on much longer timescales. However, these assumptions may not hold for long-term predictions, in which case environmental conditions, land use patterns, population distributions³¹, community compositions³², and plant functional responses³³ could all undergo significant shifts. At multidecadal to centennial timescale, slow processes such CO₂ fertilization³⁴, nutrient limitation³⁵, evolving forest demography^{36,37}, and belowground carbon dynamics^{22,38} can dominate the trajectories of land-atmosphere carbon exchange, yet most of these slow processes can be constrained only with long-term observations or by making equilibrium assumptions. In the absence of long-term global observational records on plant adaptation to climate change, the environment-parameter relationships learned from spatial gradients in this study offer insights into potential future shifts in ecosystem functions³⁹, assuming the validity of space-for-time substitution⁴⁰.

Analysis on identifiable model parameters unveiled correlations between them (Fig. 4). From a modeling perspective, inter-parameter correlation reduces the effective dimensionality of model parameters, and the sparsity of the latent parameter space is crucial for effective out-of-sample generalization in

conditions unseen in the observational record^{41–44}. Essentially, our ability to model high-dimensional physical worlds rely on the fact that most systems have much lower intrinsic dimensions governed by a few fundamental variables^{41,45–48}. Natural selection, self-organization, and entropy maximization have been proposed as three organizing principles that introduce predictability to vegetation dynamics^{2,3}, giving rise to optimality-based trait spectra of photosynthesis^{49,50}, leaf size and economics^{51–54}, plant hydraulics^{55–58}, and carbon allocations^{59–61} that reflect trade-offs under multiple selection forces.

Previous studies have leveraged dimensionality reduction algorithms on surface gas exchange measurements⁶² and global trait databases^{17,63} to extract the main axes of ecosystem traits and functions, yet they are limited by the available set of observable plant traits and uneven spatial sampling. By integrating the spatialization neural network with a differentiable TBM and assimilating diverse observations, DifferLand imposes a comprehensive set of constraints on the latent space, capturing both observed and unobserved dynamics and process dependencies. The three axes of latent parameter variations—growing season length, leaf economics, and agricultural intensity—highlight how these environment-parameter relationships influence carbon and water fluxes. It has been shown that state-of-the-art land models using PFT-based parameterizations overestimate the correlation between ecosystem functions compared with observations⁶², limiting their capacity to simulate the full diversity of ecosystem function space, such as the spatial variations of carbon-use efficiency and water use strategies, and therefore likely their response to climate change⁶². Despite its parsimonious process representation, DifferLand showcases how data-constrained hybrid differentiable modeling can be used to retrieve complex trait-environment relationships from observations, to represent the full functional diversity of vegetation-environment interactions and to unleash new science questions and answers in global carbon cycling.

Methods

DifferLand: A Hybrid-ML Terrestrial Biosphere Modeling Framework

The DifferLand configuration used in this study includes three main components: a spatialization neural network that maps spatial predictors to ecological model parameters, a process-based dynamical terrestrial biosphere model, and a loss function that computes the distance between simulated variables and observational constraints. We note that the DifferLand framework is flexible and it can accommodate different processes-based or neural network components to model ecological functional relationships⁶⁴. The spatialization network (f_{nm}) (Fig. S1) consists of first a fully-connected neural

network (FCNN) with 3 hidden-layers and 32 neurons that maps the input predictors (\mathbf{P}) to a 32-dimensional embedding. This embedding is then passed into three output layers, predicting the ecological model parameters of the Data Assimilation Linked Ecosystem Carbon (DALEC) model (θ_e , N=31), the initial pool values (θ_i , N=7), and two phenology parameters (θ_p , N=2), respectively. θ_e and θ_p together constitute the model parameters of the DALEC model (θ_M). Rectified Linear Unit (ReLU) is used at the activation function of all NN layers. NN parameters (θ_{nn}) include weights and biases in each layer, with weights are randomly initialized using the Xavier initializer⁶⁵, with biases set to one. A transform function (Text S1) is used to convert each parameter from the real space to their physical range (see Table S1 for a list of the parameters and their physical range). In mathematical form (Equation 1), the spatialization network can be expressed as

$$\theta_M^k, \theta_i^k = f_{nn}(\mathbf{P}^k | \theta_{nn}) \quad (1)$$

Where k denotes the kth pixel in spatial coverage. Note that θ_{nn} is not spatially varying, as we assume a global relationship between environmental predictors and model parameters in this hierarchical framework.

The centerpiece of DifferLand is an automatically differentiable version of the Data Assimilation Linked Ecosystem Carbon (DALEC) model, meaning that the model has the capacity to compute gradients and the sensitivity to any parameter or variable in the model with respect to a model output using back-propagation (adapted from model version 1006, see Fig. S2 for model schematics). DALEC is an intermediate-complexity dynamical terrestrial biosphere model that simulates photosynthesis, carbon allocation, leaf phenology, autotrophic and heterotrophic respiration, turnover, decomposition, and fire disturbance. Labile, foliar, wood, fine roots, litter, and soil carbon pools are prognostically computed at each time step based on mass balance principles^{9,66,67}. The model also simulates ET based on an underlying water use efficiency formulation^{68,69}, and computes a prognostic water bucket as a balance between precipitation, runoff, and ET. The water bucket feedbacks into photosynthesis to represent soil water limitation on GPP^{64,70}. Versions of the DALEC model have been used in the CARbon DATA MOdel fraMework (CARDAMOM) to conduct MDF studies at local^{66,71,72}, regional^{70,73}, to global scales⁹. At each time step t for location k, this TBM (f_M) uses meteorological forcing variables ($\mathbf{m}^{k,t}$) to prognostically evolve state variables (\mathbf{x}) and compute observable ($\overline{\mathbf{y}_o}$) and unobservable ($\overline{\mathbf{y}_u}$) ecological variables and fluxes (Equation 2). We note that at t=0, $\mathbf{x}^{k,0} = \theta_i$

$$\widehat{\mathbf{y}_o}^{k,t}, \widehat{\mathbf{y}_u}^{k,t}, \mathbf{x}^{k,t+1} = f_M(\mathbf{x}^{k,t}, \mathbf{m}^{k,t} | \theta_M^k) \quad (2)$$

Substituting (1) into (2) and considering the legacy effects of meteorological forcing on ecological states, we have

$$\widehat{\mathbf{y}}_o^{k,t}, \widehat{\mathbf{y}}_u^{k,t}, \mathbf{x}^{k,t+1} = f_M(\mathbf{m}^{k,1}, \mathbf{m}^{k,2}, \dots, \mathbf{m}^{k,t} | f_{nn}(\mathbf{P}^k | \boldsymbol{\theta}_{nn})) = f_M(\mathbf{m}^{k,1}, \mathbf{m}^{k,2}, \dots, \mathbf{m}^{k,t} | \mathbf{P}^k, \boldsymbol{\theta}_{nn}) \quad (3)$$

Equation 3 essentially states that the ecological fluxes at states any time and location is a function of the environmental background (\mathbf{P}^k), the environment-parameter relationships learned through the spatialization network ($\boldsymbol{\theta}_{nn}$), the current and legacy meteorological forcings up to that time ($\mathbf{m}^{k,1}, \mathbf{m}^{k,2}, \dots, \mathbf{m}^{k,t}$), and the ecological process dependencies encoded in the TBM (f_M).

By selecting a parsimonious TBM, we aim to include mechanistic representations that capture essential ecological processes while minimizing equifinality and the high computational costs associated with more sophisticated models. Despite its relative simplicity, DALEC has shown strong performance in capturing global carbon flux dynamics within ranges comparable to much more complex Dynamic Global Vegetation Models (DGVMs) and fully-coupled Earth System Models (ESMs)⁷⁴. A brief summary of the DALEC model can be found in [Text S2](#), and additional details about the adaptations made to convert DALEC into a differentiable model has been described in previous work⁶⁴.

The loss function (equation 4) calculates a weighted sum of mean squared error (MSE) between model simulated ($\widehat{\mathbf{y}}_o$) and observed (\mathbf{y}_o) NEE, LAI, SIF, ET, RECO, VOD, live biomass, fire C emission, and soil organic carbon from gridded datasets. It also compares the differences between simulated and observed GPP, RECO, and ET at a global network of eddy covariance sites where grid cells overlap with tower sites ([Fig. S2](#)). Among the variables that are not directly simulated by DALEC but assimilated to inform carbon dynamics, (reconstructed) SIF is assumed to have a linear relationship between modeled GPP at monthly level⁷⁵, with the slope and intercept of the GPP-SIF relationships treated as model parameters to be predicted from the spatialization neural network⁷⁰. L-band VOD⁷⁶ is considered to be composed of signals derived from a linear combination of foliar and wood biomass⁷⁷, with the coefficients to be estimated spatially within numerical bounds designed to untangle their contributions⁷⁸. Live biomass was computed as the sum of the labile, foliar, wood, and fine roots carbon pools. In addition, we included a constraint term to prevent excessive drying of the water pool, as this was previously found important for predicting water dynamics in semi-arid regions⁶⁴.

$$\mathcal{L} = \sum_{k,t,v} \alpha_v (\widehat{\mathbf{y}}_o^{k,t,v} - \mathbf{y}_o^{k,t,v})^2 \quad (4)$$

Index v denotes the v^{th} variable in the loss function. The gradient of the loss function with respect to the NN parameters in the spatialization network (θ_{nn}) is used to optimize the entire framework. We heuristically tuned the weights for different loss terms (α_v) to achieve a balanced performance on all observational constraints. The complete set of hyperparameters used in this study are listed in [Table S2](#). We implemented DifferLand in JAX⁷⁹, an automatic differentiation software package built in Python. All code and data used in this study can be accessed with the links provided in the Code & Data Availability section.

Datasets

DifferLand requires three types of data inputs: spatial predictors (\mathbf{P}), forcing variables (\mathbf{m}), and observational constraints (\mathbf{y}_o).

Spatial predictors

Spatial variables are classified into four groups: PFT, CLIM, AGE, and SOIL (i.e., $\mathbf{P} \subseteq \{PFT, CLIM, SOIL, AGE\}$). PFT variables are derived from MCD12C1.v061 MODIS/Terra + Aqua Yearly Land Cover Type⁸⁰, with the percentage of underlying 500m classes aggregated to 0.25° grid cells. We consolidated the International Geosphere Biosphere Programme (IGBP) fractions into 11 classes including needleleaf forest (ENF+DNF), deciduous broadleaf forest (DBF), evergreen broadleaf forest (EBF), mixed forest (MF), shrubland (SH), savanna (WSA+OSA), grassland (GRA), wetland (WET), cropland (CRO+CNM), and a non-vegetated land surface class encompassing all other land cover types (URB+SNO+BSV). Pixels where the area of permanent water bodies exceeds 50% or non-vegetated surface exceeds 20%, were excluded from the analysis.

The CLIM group includes mean annual temperature (MAT, °C) and mean annual precipitation (MAP, mm) averaged over 2010-2023 from ERA5 reanalysis by ECMWF⁸¹. We also elevation (ELE, m) derived from the Global 30 Arc-Second Elevation dataset (GTOPO30)^{82,83}.

The AGE predictor group includes forest age (year) estimates obtained from a global 1 km forest age dataset (circa 2010)^{84,85}, which used a machine learning algorithm and data from more than 40,000 forest inventory plots to estimate global forest age. We used tree age estimates with 10% tree cover correction for our analysis, whereas non-forest pixels were assigned an age value of 1 year assuming annual vegetation turnover. Also in this group is the maximum canopy height (CAN.H, m) from the ETH

Global Sentinel-2 10 m Canopy Height dataset⁸⁶, accessed from Google Earth Engine. We first computed the 95th-percentile canopy height at 1 km spatial resolution to represent forest growth potential while avoiding single pixel outliers, followed by calculating maximum value among the 1 km pixels within each 0.25° grid cell.

SOIL predictors include soil bulk density and soil sand, silt, clay, and gravel fractions derived from the Regridded Harmonized World Soil Database v1.2⁸⁷ available at 0.05° resolution. We combined surface soil (0-30cm) and deeper soil values (30-100cm) to a top 1m value(0-100cm) by computing a depth weighted mean. All spatial predictors are assumed to be temporally invariant and converted to a common spatial resolution of 0.25°.

Forcing data

Monthly-averaged forcing data used to drive the DALEC model include daily min temperature (°C), daily max temperature (°C), shortwave solar radiation downward (W/m²), precipitation rate (mm/day), and VPD (kPa) computed from ERA5 Reanalysis⁸¹ between 2010-2023 at 0.25° resolution. Globally-averaged monthly CO₂ concentration (ppm) was obtained from NOAA Global Monitoring Laboratory measurements⁸⁸. Fire dynamics were driven by burned area from the Fifth Version of Global Fire Emissions Database (GFED5)⁸⁹ at 0.25° resolution between 2010 and 2020. We divided the burned area by the burnable area estimated in GFED5 to obtain burned area fraction. As GFED data since 2021 is still not available, we repeated the monthly mean seasonal cycle between 2018 and 2020 for 2021-2023.

Observational constraints

We assimilated 12 globally gridded or in-situ datasets to constrain various aspects of the terrestrial biosphere represented in DifferLand (Fig. S2). We used 0.05° biweekly Long-term Reconstructed Solar-Induced Fluorescence (LRSIF) as a proxy of GPP between 2010-2023^{90,91}. Reprocessed MODIS Version 6.1 Leaf Area Index^{92,93}, which exhibited enhanced spatial and temporal continuity compared with the original MCD15A2H, was used to constrain modeled foliar dynamics from 2010-2021. Evapotranspiration from Global Land Evaporation Amsterdam Model (GLEAM) v4.1a at 0.1° resolution was used to constrain modeled ET between 2010-2023⁹⁴. The L-Band AI-Based GLAB-VOD from 2010-2020 was used to constrain the foliar and wood dynamics^{76,77}. The aforementioned global datasets were regridded to 0.25° grid cells at monthly intervals to match DifferLand output.

Annual live woody biomass (B_w) maps from 2010-2019 were obtained from a dataset reconstructed with an array of inventory plots, airborne, and satellite observations⁹⁵. Herbaceous biomass (B_h) is estimated under an equilibrium assumption with $B_h = f_h \times \overline{GPP} / \tau \times (1 - \alpha)$, where f_h is the area fraction of herbaceous vegetation within each grid cell estimated from MCD12C1, \overline{GPP} is annual GPP climatology estimated from FLUXCOM upscaling⁹⁶, α is respiration cost of carbon (assumed to be 0.5), and τ is the mean residence time taken as one year for annual plants⁹⁷. Total live biomass (B_l) is computed as $B_l = B_h + B_w$. In the absence of temporal observations, this use of equilibrium assumption provides an estimate of the spatial gradient of live biomass density. The lack of temporal variability in biomass estimates is partially compensated by assimilated LAI and VOD dynamics in those regions. We aggregated annual live biomass density to a 0.25° spatial resolution.

Monthly NBE from the NASA Carbon Monitoring System Flux (CMS-Flux) GCP 2023 submission⁹⁸⁻¹⁰⁰ was used to constrain DifferLand modeled NBE from 2010-2022. CMS-Flux is a top-down flux inversion system constrained by column CO_2 observations from the Greenhouse Gases Observing Satellite (GOSAT) and Observing Carbon Observatory-2 (OCO-2), which have broader and more even spatial coverage compared with ground-based CO_2 observations^{101,102}. Due to the computational cost of the atmospheric transport model, CMS-Flux has a native resolution of $4^\circ \times 5^\circ$. We also assimilated fire carbon emission using the CMS Carbon Flux for Fire¹⁰³ inversion between 2010 and 2016, informed by satellite column CO concentration measurements from MOPITT¹⁰⁴. To constrain DifferLand simulated terrestrial water storage, we assimilated monthly satellite-gravimetry based JPL GRACE and GRACE-FO Mascon Equivalent Water Height (GRACE EWT) from 2010-2022 (Release 06.1 Version 03)¹⁰⁵. Although GRACE EWT was provided in 0.5° grids, the product has an effective resolution of $3^\circ \times 3^\circ$. We thus assimilated both CMS-Flux NBE and GRACE EWT at the $4^\circ \times 5^\circ$ batch level to prevent signal aliasing (see the next section for details).

We also assembled monthly eddy-covariance based observations GPP, RECO, and ET by combining the FLUXNET2015¹⁰⁶, ICOS¹⁰⁷, and AmeriFlux FLUXNET datasets. For GPP and RECO, we used night-time partitioned values with variable u^* threshold and removed months where more than 30% of the NEE measurements were gap-filled¹⁰⁸. For ET, we removed months where more than 30% of the latent heat flux measurements were gap-filled. After filtering, we retained 187 sites with more than 12 months of observations for all three variables during the simulation period. Whenever available, we gridded the

site-level data to 0.25°. If observations from multiple sites within a grid cell were available in a specific month, we used the mean value across these sites to fill the grid cell. A complete list of the eddy covariance sites used in this study is provided in SI [Table S3](#).

Model Training & Evaluation

To assimilate multi-resolution observational constraints at both fine (0.25°) and coarse (4°x5°) resolutions, we first divided the globe into 3240 4°x5° patches, each corresponding to the grid of coarse-resolution datasets. Each 4°x5° patch contains 320 nested fine-resolution grid cells ([Fig. S3](#)). We filtered these patches to retain only those with at least 32 valid vegetated fine-resolution grid cells. Out of the 939 patches meeting this criterion, 10% of the patches (N = 94) were randomly selected and reserved for model testing ([Fig. S3c](#)). Prior to training each ensemble, we randomly sampled 90% of the remaining 845 patches for training, while the unselected patches formed a development set used for hyperparameter tuning and monitoring training progress ([Fig. S3a](#)). The final training set contains 164,040 grid cells with a total of 27,558,720 pixel-months. All spatial predictors were standardized by subtracting their means and dividing by their standard deviations, calculated from the training dataset, to accelerate model convergence.

We developed a customized stochastic gradient descent algorithm to train the multi-resolution model. This approach first permutes the fine-resolution grids within each patch and then shuffles the patches within the training set to introduce stochasticity, while ensuring that all fine-resolution grid cells within a patch remain grouped. As a result, each patch forms a minibatch (batch size = 320) during model training, allowing fine-resolution datasets to serve as sample-level constraints, and coarse-resolution datasets as batch-level constraints. We assimilate coarse resolution constraints at the patch level only if at least 80% of the fine resolution grid cells within the patch are valid. The model was trained using the Adam optimizer, with a learning rate of 0.0005. Each ensemble member underwent 199 epochs of training, a choice balanced between computational cost, model convergence, and mitigating overfitting risks.

After training, we evaluated model performance on the held-out test datasets. We used R²-score as a measure of overall model fitting on each variable

$$R^2 = 1 - \frac{\sum_{i=1}^n (y_i - \hat{y}_i)^2}{\sum_{i=1}^n (y_i - \bar{y})^2}$$

With y_i being i^{th} observed value, \hat{y}_i being the i^{th} modeled value, and \bar{y} is the observed mean. The R^2 -score is mathematically equivalent to the Nash-Sutcliffe Efficiency (NSE) metric commonly used in hydrology, which accounts for both correlation and systematic offsets between modeled and observed values. A perfect model would have $R^2=1$, but the R^2 -score can approach $-\text{Inf}$ for arbitrarily bad predictions. Thus, we also used the explained variance score (r^2), computed as the square of the Pearson correlation coefficient between modeled and observed values (range 0-1), for hierarchical partition and pixelwise temporal correlations. We made explicit in our manuscript which metric was used when reporting the results.

Hierarchical Partition of Explained Variance

Hierarchical partition²⁶ enables a decomposition of the explained variance on target variables by a multivariate regression model into the independent contributions of different groups of variables. To segregate the independent contributions of PFT, CLIM, SOIL, and AGE, we performed a full factorial experiment by including or excluding each group of variables, resulting in a total of 16 setups (i.e., $|\mathcal{P}(\{\text{PFT, CLIM, SOIL, AGE}\})|=2^4$, where $\mathcal{P}(\cdot)$ denotes power set). A CONTROL setup using only a white noise variable (as a null predictor) represents the model baseline without parameter spatialization, as any predictability of observed variables could only originate from model structure and forcing variables. In addition, we also included a separate control case where only latitude and longitude are used as spatial predictors (LATLON). This setup served as a sanity check to ensure that DifferLand is capable of learning ecologically meaningful relationships from the predictors, rather than merely interpolating using the spatial autocorrelation embedded in the datasets.

For each setup, we ran 20 experiments with random initializations and selected the 10 with the lowest training loss, minimizing the impact of poor initializations and forming a robust model ensemble. The mean performance metric across these 10 ensemble members is used to represent a setup. Under the hierarchical theorem, the independent effect of a variable group j within a set containing N groups of variables can be computed as the mean explained variance (or R^2) difference between N pairs of setups within a predictor group hierarchy where j is either included or excluded from the predictor set, averaged over all possible $(N-1)!$ sequences of hierarchies²⁶. We conducted a hierarchical partitioning analysis on both explained variance and R^2 for SIF, LAI, ET, NEE, and EWT at the global level, and on explained variance at the pixel level. We then derived the proportion of explained variance (or R^2) that

can be independently attributed to each predictor group or model structure & forcing at local and global levels.

Parameter Identifiability Analysis

We conducted parameter identifiability analyses on the two setups using either the full set of predictors (PFT+CLIM+SOIL+AGE) or all of the non-PFT predictors (CLIM+SOIL+AGE). To ensure the robustness of the results, we trained 30 additional model ensembles for these two setups, and selected 25 out of 50 runs with the best training loss to form the ensembles. For each model parameter and initial pool value, we computed the pixelwise coefficient of variance (CV) across ensemble members and used the spatial median CV as a diagnostic for predictor robustness. The rationale of this test is that if a latent ecological parameter is well constrained by the assimilated observations, it should converge to relatively stable values across independently initialized runs. Conversely, non-identifiable parameters with low sensitivity to the observational constraints can be expected to take substantially different values across independently initialized runs. We used spatial median CV <0.5 as a threshold to define identifiable parameters.

Principal Component Analysis (PCA) on Ecological Parameters

We performed a principal component analysis (PCA) on 13 ecologically significant and spatially consistent parameters to determine the underlying dimensions controlling their spatial variability. These parameters include canopy photosynthetic efficiency (ce), underlying water use efficiency ($uWUE$), temperature sensitivity of heterotrophic respiration (Q_{10}), autotrophic respiration fraction (A_{auto}), leaf carbon mass per area (LCMA), leaf onset (c_{ronset}) and fall duration (c_{rfall}), leaf lifespan (τ_{foliar}), and allocation fraction of GPP to labile (A_{labile}), foliar (A_{foliar}), wood (A_{wood}), and fine roots (A_{root}) pools. Overall, these parameters characterize ecosystem functions related to photosynthesis & leaf phenology, carbon allocation, residence time, and water use efficiency. We projected these parameters into the space defined by the first three principal components to explore their interrelationships (Fig. 4a). Additionally, we mapped the spatial patterns of the first three principal components to further investigate their spatial patterns (Fig. 4b-d).

SHAP Analysis for Feature Importance & Environment-Parameter Relationships

We applied kernel SHapley Additive exPlanations (SHAP) to extract the learned environment-parameter relationship from the spatialization neural network for a selection of latent ecological parameters¹⁰⁹.

Kernel SHAP estimates Shapley values, informed by cooperative game theory, to quantify each feature's marginal and additive contribution to the model's output. We sampled 100 grid cells to compute the background distribution, and then computed the SHAP values from 1000 randomly selected grid cells within the training dataset. Feature importance of different predictors ranked by the mean absolute SHAP values from the 1000 samples. We then plotted SHAP values against feature values for the top three predictors to examine the functional form of environment-parameter relationships.

Code & Data Availability

The code of the DifferLand model is available at https://github.com/JianingFang/DifferLand_Global (code uploaded as a zip file for peer-review). The driver files used for the DifferLand model is stored at [doi:10.5281/zenodo.13984226](https://doi.org/10.5281/zenodo.13984226). Both the code and data will be available to the public at publication.

Conflicts of Interests

The authors declare no competing interests.

Acknowledgements

We would like to express our appreciation for Dr. Nuno Carvalhais and members of the Model-Data Integration group at the Max Planck Institute for Biogeochemistry (MPI-BGC) for the insightful discussions related to this work during J.F.'s academic visit. J.F. and P.G. are supported by the NASA ROSES-22 Future Investigators in NASA Earth and Space Science and Technology (FINESST) Program (Grant Number: 80NSSC24K0023). This work was also funded by the Land Ecosystem Models based On New Theory, observations, and Experiments (LEMONTREE) project (UREAD 1005109-LEMONTREE), the European Research Council grant USMILE (ERC CU18-3746), the Max-Planck Caltech Carnegie Columbia (MC³) Center funded by the Max Planck Foundation, and National Science Foundation Science and Technology Center LEAP, Learning the Earth with Artificial intelligence and Physics (AGS-2019625).

References

1. Carpenter, S. R. & Turner, M. G. Hares and Tortoises: Interactions of Fast and Slow Variables in Ecosystems. *Ecosystems* **3**, 495–497 (2001).
2. Franklin, O. *et al.* Organizing principles for vegetation dynamics. *Nat. Plants* **6**, 444–453 (2020).

3. Harrison, S. P. *et al.* Eco-evolutionary optimality as a means to improve vegetation and land-surface models. *New Phytologist* **231**, 2125–2141 (2021).
4. McIntyre, S., Lavorel, S., Landsberg, J. & Forbes, T. D. A. Disturbance Response in Vegetation: Towards a Global Perspective on Functional Traits. *Journal of Vegetation Science* **10**, 621–630 (1999).
5. Luo, Y. & Smith, B. *Land Carbon Cycle Modeling: Matrix Approach, Data Assimilation, & Ecological Forecasting*. (CRC Press, 2022).
6. Keenan, T. F. & Williams, C. A. The Terrestrial Carbon Sink. *Annual Review of Environmental Resources* **43**, 219–243 (2018).
7. Cranko Page, J., Abramowitz, G., De Kauwe, Martin. G. & Pitman, A. J. Are Plant Functional Types Fit for Purpose? *Geophysical Research Letters* **51**, e2023GL104962 (2024).
8. Fisher, R. A. & Koven, C. D. Perspectives on the Future of Land Surface Models and the Challenges of Representing Complex Terrestrial Systems. *Journal of Advances in Modeling Earth Systems* **12**, e2018MS001453 (2020).
9. Bloom, A. A., Exbrayat, J.-F., Van Der Velde, I. R., Feng, L. & Williams, M. The decadal state of the terrestrial carbon cycle: Global retrievals of terrestrial carbon allocation, pools, and residence times. *Proceedings of the National Academy of Sciences* **113**, 1285–1290 (2016).
10. Wright, I. J. *et al.* Assessing the generality of global leaf trait relationships. *New Phytologist* **166**, 485–496 (2005).
11. Liu, Y. *et al.* Canopy Height and Climate Dryness Parsimoniously Explain Spatial Variation of Unstressed Stomatal Conductance. *Geophysical Research Letters* **49**, e2022GL099339 (2022).
12. Liu, Y., Holtzman, N. M. & Konings, A. G. Global ecosystem-scale plant hydraulic traits retrieved using model–data fusion. *Hydrology and Earth System Sciences* **25**, 2399–2417 (2021).
13. Xu, X. & Trugman, A. T. Trait-Based Modeling of Terrestrial Ecosystems: Advances and Challenges Under Global Change. *Curr Clim Change Rep* **7**, 1–13 (2021).

14. Butler, E. E. *et al.* Mapping local and global variability in plant trait distributions. *Proc. Natl. Acad. Sci. U.S.A.* **114**, (2017).
15. Yang, H. *et al.* Variations of carbon allocation and turnover time across tropical forests. *Global Ecol Biogeogr* **30**, 1271–1285 (2021).
16. Famiglietti, C. A. *et al.* Global net biome CO₂ exchange predicted comparably well using parameter–environment relationships and plant functional types. *Global Change Biology* **29**, 2256–2273 (2023).
17. Joswig, J. S. *et al.* Climatic and soil factors explain the two-dimensional spectrum of global plant trait variation. *Nat Ecol Evol* **6**, 36–50 (2021).
18. Anderegg, L. D. L. Why can't we predict traits from the environment? *New Phytologist* **237**, 1998–2004 (2023).
19. Meyer, H. & Pebesma, E. Machine learning-based global maps of ecological variables and the challenge of assessing them. *Nat Commun* **13**, 2208 (2022).
20. Luo, Y. *et al.* Ecological forecasting and data assimilation in a data-rich era. *Ecological Applications* **21**, 1429–1442 (2011).
21. Tao, F. & Luo, Y. PROcess-guided deep learning and DAta-driven modelling (PRODA). in *Land Carbon Cycle Modeling* 319–328 (CRC Press, 2022).
22. Tao, F. *et al.* Microbial carbon use efficiency promotes global soil carbon storage. *Nature* (2023) doi:10.1038/s41586-023-06042-3.
23. Norton, A. J. *et al.* Improved process representation of leaf phenology significantly shifts climate sensitivity of ecosystem carbon balance. *Biogeosciences* **20**, 2455–2484 (2023).
24. Girardin, C. A. J. *et al.* Seasonal trends of Amazonian rainforest phenology, net primary productivity, and carbon allocation: Seasonal Trends of Amazonian Forests. *Global Biogeochem. Cycles* **30**, 700–715 (2016).

25. Lopes, A. P. *et al.* Leaf flush drives dry season green-up of the Central Amazon. *Remote Sensing of Environment* **182**, 90–98 (2016).
26. Chevan, A. & Sutherland, M. Hierarchical Partitioning. (2024).
27. Collalti, A. & Prentice, I. C. Is NPP proportional to GPP? Waring’s hypothesis 20 years on. *Tree Physiology* **39**, 1473–1483 (2019).
28. Hongyan, Z. Global pattern of NPP to GPP ratio derived from MODIS data: effects of ecosystem type, geographical location and climate. *Global Ecology and Biogeography* (2008).
29. Zhou, T., Shi, P., Hui, D. & Luo, Y. Global pattern of temperature sensitivity of soil heterotrophic respiration (Q₁₀) and its implications for carbon-climate feedback. *Journal of Geophysical Research: Biogeosciences* **114**, (2009).
30. Moreno-Martínez, Á. *et al.* A methodology to derive global maps of leaf traits using remote sensing and climate data. *Remote Sensing of Environment* **218**, 69–88 (2018).
31. Kelly, A. E. & Goulden, M. L. Rapid shifts in plant distribution with recent climate change. *Proc. Natl. Acad. Sci. U.S.A.* **105**, 11823–11826 (2008).
32. Liu, H. *et al.* Shifting plant species composition in response to climate change stabilizes grassland primary production. *Proc. Natl. Acad. Sci. U.S.A.* **115**, 4051–4056 (2018).
33. Franks, S. J., Weber, J. J. & Aitken, S. N. Evolutionary and plastic responses to climate change in terrestrial plant populations. *Evolutionary Applications* **7**, 123–139 (2014).
34. Quetin, G. R. *et al.* Attributing past carbon fluxes to CO₂ and climate change: Respiration response to CO₂ fertilization shifts regional distribution of the carbon sink. *Global Biogeochemical Cycles* (2023) doi:10.1029/2022GB007478.
35. Terrer, C. *et al.* Nitrogen and phosphorus constrain the CO₂ fertilization of global plant biomass. *Nat. Clim. Chang.* **9**, 684–689 (2019).
36. Robinson, N. *et al.* Protect young secondary forests for optimum carbon removal. (2024).

37. Yang, H. *et al.* Global increase in biomass carbon stock dominated by growth of northern young forests over past decade. *Nat. Geosci.* **16**, 886–892 (2023).
38. Huang, Y. *et al.* Size, distribution, and vulnerability of the global soil inorganic carbon. *Science* **384**, 233–239 (2024).
39. Space-for-Time Substitution as an Alternative to Long-Term Studies. in *Long-Term Studies in Ecology* 110–135 (Springer New York, New York, NY, 1989). doi:10.1007/978-1-4615-7358-6_5.
40. Damgaard, C. A Critique of the Space-for-Time Substitution Practice in Community Ecology. *Trends in Ecology & Evolution* **34**, 416–421 (2019).
41. Chen, B. *et al.* Automated discovery of fundamental variables hidden in experimental data. *Nat Comput Sci* **2**, 433–442 (2022).
42. Floryan, D. & Graham, M. D. Data-driven discovery of intrinsic dynamics. *Nat Mach Intell* **4**, 1113–1120 (2022).
43. Brunton, S. L., Proctor, J. L. & Kutz, J. N. Discovering governing equations from data by sparse identification of nonlinear dynamical systems. *Proc. Natl. Acad. Sci. U.S.A.* **113**, 3932–3937 (2016).
44. Champion, K., Lusch, B., Nathan Kutz, J. & Brunton, S. L. Data-driven discovery of coordinates and governing equations. *Proceedings of the National Academy of Sciences of the United States of America* **116**, 22445–22451 (2019).
45. Famiglietti, C. A. *et al.* Optimal model complexity for terrestrial carbon cycle prediction. *Biogeosciences* **18**, 2727–2754 (2021).
46. Buckingham, E. On physically similar systems; illustrations of the use of dimensional equations. *Physical review* **4**, 345 (1914).
47. Porporato, A. Hydrology without dimensions. *Hydrol. Earth Syst. Sci.* **26**, 355–374 (2022).
48. Feng, X. *et al.* The ecohydrological context of drought and classification of plant responses. *Ecology Letters* **21**, 1723–1736 (2018).

49. Prentice, I. C., Dong, N., Gleason, S. M., Maire, V. & Wright, I. J. Balancing the costs of carbon gain and water transport: testing a new theoretical framework for plant functional ecology. *Ecology Letters* **17**, 82–91 (2014).
50. Joshi, J. *et al.* Towards a unified theory of plant photosynthesis and hydraulics. *Nat. Plants* **8**, 1304–1316 (2022).
51. De La Riva, E. G. *et al.* A plant economics spectrum in Mediterranean forests along environmental gradients: is there coordination among leaf, stem and root traits? *J Vegetation Science* **27**, 187–199 (2016).
52. Dong, N., Dechant, B., Wang, W., Wright, I. J. & Prentice, I. C. Global leaf-trait mapping based on optimality theory. *Global Ecol Biogeogr* **32**, 1152–1162 (2023).
53. Wang, H. *et al.* Leaf economics fundamentals explained by optimality principles. *Sci. Adv.* **9**, eadd5667 (2023).
54. Wright, I. J. *et al.* Global climatic drivers of leaf size. *Science* **357**, 917–921 (2017).
55. Xu, H., Wang, H., Prentice, I. C., Harrison, S. P. & Wright, I. J. Plant hydraulics coordinated with photosynthetic traits and climate. Preprint at <https://doi.org/10.1101/2021.03.02.433324> (2021).
56. Anderegg, W. R. L. *et al.* Woody plants optimise stomatal behaviour relative to hydraulic risk. *Ecology Letters* **21**, 968–977 (2018).
57. Mencuccini, M., Minunno, F., Salmon, Y., Martínez-Vilalta, J. & Hölttä, T. Coordination of physiological traits involved in drought-induced mortality of woody plants. *New Phytologist* **208**, 396–409 (2015).
58. Franklin, O., Fransson, P., Hofhansl, F., Jansen, S. & Joshi, J. Optimal balancing of xylem efficiency and safety explains plant vulnerability to drought. *Ecology Letters* **26**, 1485–1496 (2023).
59. De La Riva, E. G. *et al.* The Economics Spectrum Drives Root Trait Strategies in Mediterranean Vegetation. *Front. Plant Sci.* **12**, 773118 (2021).

60. Schymanski, S. J., Sivapalan, M., Roderick, M. L., Beringer, J. & Hutley, L. B. An optimality-based model of the coupled soil moisture and root dynamics. *Hydrology and Earth System Sciences* **12**, 913–932 (2008).
61. Gentine, P., D’Odorico, P., Lintner, B. R., Sivandran, G. & Salvucci, G. Interdependence of climate, soil, and vegetation as constrained by the Budyko curve. *Geophysical Research Letters* **39**, (2012).
62. Migliavacca, M. *et al.* The three major axes of terrestrial ecosystem function. *Nature* (2021) doi:10.1038/s41586-021-03939-9.
63. Díaz, S. *et al.* The global spectrum of plant form and function. *Nature* **529**, 167–171 (2016).
64. Fang, J. & Gentine, P. Exploring Optimal Complexity for Water Stress Representation in Terrestrial Carbon Models: A Hybrid-Machine Learning Model Approach. *Authorea Preprints* (2024).
65. Glorot, X. & Bengio, Y. Understanding the difficulty of training deep feedforward neural networks. in *Proceedings of the Thirteenth International Conference on Artificial Intelligence and Statistics* 249–256 (JMLR Workshop and Conference Proceedings, 2010).
66. Bloom, A. A. & Williams, M. Constraining ecosystem carbon dynamics in a data-limited world: Integrating ecological ‘common sense’ in a model-data fusion framework. *Biogeosciences* **12**, 1299–1315 (2015).
67. Williams, M., Schwarz, P. A., Law, B. E., Irvine, J. & Kurpius, M. R. An improved analysis of forest carbon dynamics using data assimilation. *Global Change Biology* **11**, 89–105 (2005).
68. Zhou, S., Yu, B., Huang, Y. & Wang, G. Daily underlying water use efficiency for AmeriFlux sites. *Journal of Geophysical Research: Biogeosciences* **120**, 887–902 (2015).
69. Boese, S., Jung, M., Carvalhais, N., Teuling, A. J. & Reichstein, M. Carbon-water flux coupling under progressive drought. *Biogeosciences* **16**, 2557–2572 (2019).
70. Levine, P. A. *et al.* Water Stress Dominates 21st-Century Tropical Land Carbon Uptake. *Global Biogeochemical Cycles* **37**, e2023GB007702 (2023).

71. Worden, M. A. *et al.* Inferred drought-induced plant allocation shifts and their impact on drought legacy at a tropical forest site. *Global Change Biology* **30**, e17287 (2024).
72. Yang, Y. *et al.* CARDAMOM-FluxVal version 1.0: a FLUXNET-based validation system for CARDAMOM carbon and water flux estimates. *Geosci. Model Dev.* **15**, 1789–1802 (2022).
73. Williams, M. Global Carbon Cycle Data Assimilation Using Earth Observation: The CARDAMOM Approach. in *Land Carbon Cycle Modeling* 225–235 (CRC Press, 2022).
74. Quetin, G. R., Bloom, A. A., Bowman, K. W. & Konings, A. G. Carbon Flux Variability From a Relatively Simple Ecosystem Model With Assimilated Data Is Consistent With Terrestrial Biosphere Model Estimates. *J Adv Model Earth Syst* **12**, (2020).
75. Sun, Y. *et al.* From remotely-sensed solar-induced chlorophyll fluorescence to ecosystem structure, function, and service: Part II—Harnessing data. *Global Change Biology* **29**, 2893–2925 (2023).
76. Skulovich, O., Gentine, P., Wigneron, J. P. & Xiaojun, L. GLAB-VOD: Global L-band AI-Based Vegetation Optical Depth Dataset Based on Machine Learning and Remote Sensing. Zenodo <https://doi.org/10.5281/zenodo.10306094> (2024).
77. Skulovich, O., Li, X., Wigneron, J.-P. & Gentine, P. Global L-band equivalent AI-based vegetation optical depth dataset. *Sci Data* **11**, 936 (2024).
78. Skulovich, O., Famiglietti, C., Konings, A. & Gentine, P. *Constraining Respiration Flux and Carbon Pools in a Simple Ecosystem Carbon Model.*
<https://www.authorea.com/users/721724/articles/706730-constraining-respiration-flux-and-carbon-pools-in-a-simple-ecosystem-carbon-model?commit=7c23d07cb2364145d59a94fc92e59db111410c9b> (2024)
doi:10.22541/au.170708964.48441645/v1.
79. Bradbury, J. *et al.* JAX: composable transformations of Python+ NumPy programs. (2018).

80. Friedl, M. & Sulla-Menashe, D. MODIS/Terra+Aqua Land Cover Type Yearly L3 Global 0.05Deg CMG V061. <https://doi.org/10.5067/MODIS/MCD12C1.061> (2022).
81. Hersbach, H. *et al.* ERA5 hourly data on single levels from 1940 to present. Copernicus Climate Change Service (C3S) Climate Data Store (CDS) (2023).
82. USGS EROS Data Center. Global 30 Arc-Second Elevation (GTOPO30). <https://doi.org/10.5066/F7DF6PQS> (1996).
83. Gesch, D. B., Verdin, K. L. & Greenlee, S. K. New land surface digital elevation model covers the Earth. *Eos, Transactions American Geophysical Union* **80**, 69–70 (1999).
84. Besnard, S. *et al.* Global 1km forest age datasets. BGI Data Portal <https://doi.org/10.17871/ForestAgeBGI.2021> (2021).
85. Besnard, S. *et al.* Mapping global forest age from forest inventories, biomass and climate data. *Earth System Science Data* **13**, 4881–4896 (2021).
86. Lang, N., Jetz, W., Schindler, K. & Wegner, J. D. A high-resolution canopy height model of the Earth. *Nat Ecol Evol* **7**, 1778–1789 (2023).
87. Wieder, W. R., Boehnert, J., Bonan, G. B. & Langseth, M. RegridDED Harmonized World Soil Database v1.2. Oak Ridge National Laboratory Distributed Active Archive Center <https://doi.org/10.3334/ORNLDAAAC/1247> (2014).
88. Lan, X., Tans, P. & Thoning, K. W. Trends in globally-averaged CO₂ determined from NOAA Global Monitoring Laboratory measurements. <https://doi.org/10.15138/9N0H-ZH07> (2024).
89. Chen, Y. *et al.* Multi-decadal trends and variability in burned area from the fifth version of the Global Fire Emissions Database (GFED5). *Earth System Science Data* **15**, 5227–5259 (2023).
90. Fang, J. *et al.* A Reconstruction of Long-Term Spatially Contiguous Solar-Induced Fluorescence Proxy over 2001-2022 Using MODIS Surface Reflectance (LCSIF-MODIS). Zenodo <https://doi.org/10.5281/zenodo.13922379> (2024).

91. Fang, J. *et al.* Reconstruction of a long-term spatially contiguous solar-induced fluorescence (LCSIF) over 1982-2022. *arXiv preprint arXiv:2311.14987* (2023).
92. Lin, W. *et al.* Reprocessed MODIS Version 6.1 Leaf Area Index dataset. 4TU.ResearchData <https://doi.org/10.4121/21858717.v2> (2023).
93. Lin, W. *et al.* Reprocessed MODIS Version 6.1 Leaf Area Index Dataset and Its Evaluation for Land Surface and Climate Modeling. *Remote Sensing* **15**, 1780 (2023).
94. Miralles, D. G. *et al.* GLEAM4: global evaporation and soil moisture datasets at 0.1° resolution from 1980 to near present.
95. Xu, L. *et al.* Changes in global terrestrial live biomass over the 21st century. *Sci. Adv.* **7**, eabe9829 (2021).
96. Jung, M. *et al.* Scaling carbon fluxes from eddy covariance sites to globe: synthesis and evaluation of the FLUXCOM approach. *Biogeosciences* **17**, 1343–1365 (2020).
97. Fan, N. *et al.* Global apparent temperature sensitivity of terrestrial carbon turnover modulated by hydrometeorological factors. *Nat. Geosci.* **15**, 989–994 (2022).
98. Friedlingstein, P. *et al.* Global carbon budget 2023. *Earth System Science Data* **15**, 5301–5369 (2023).
99. Liu, J. *et al.* Carbon Monitoring System Flux Net Biosphere Exchange 2020 (CMS-Flux NBE 2020). *Earth System Science Data* **13**, 299–330 (2021).
100. Liu, J. CMS-Flux GCP 2023 Submission. (2024).
101. Liu, J. *et al.* Carbon monitoring system flux estimation and attribution: impact of ACOS-GOSAT XCO₂ sampling on the inference of terrestrial biospheric sources and sinks. *Tellus B: Chemical and Physical Meteorology* **66**, 22486 (2014).
102. Liu, J. *et al.* Contrasting carbon cycle responses of the tropical continents to the 2015–2016 El Niño. *Science* **358**, eaam5690 (2017).

103. Bowman, K. Carbon Monitoring System Carbon Flux for Fire L4 V2 (CMSFluxFire).
<https://doi.org/10.5067/HO07ZJEQBMHE> (2020).
104. Bowman, K. W. *et al.* Global and Brazilian Carbon Response to El Niño Modoki 2011–2010. *Earth and Space Science* **4**, 637–660 (2017).
105. Wiese, D. N., Yuan, D.-N., Boening, C., Landerer, F. W. & Watkins, M. M. JPL GRACE and GRACE-FO Mascon Ocean, Ice, and Hydrology Equivalent Water Height CRI Filtered. Physical Oceanography Distributed Active Archive Center <https://doi.org/10.5067/TEMSC-3JC63> (2023).
106. Pastorello, G. *et al.* The FLUXNET2015 dataset and the ONEFlux processing pipeline for eddy covariance data. *Scientific data* **7**, 225 (2020).
107. Warm Winter 2020 Team & ICOS Ecosystem Thematic Centre. Warm Winter 2020 ecosystem eddy covariance flux product for 73 stations in FLUXNET-Archive format—release 2022-1 (Version 1.0). ICOS Carbon Portal <https://doi.org/10.18160/2G60-ZHAK> (2022).
108. Reichstein, M. *et al.* On the separation of net ecosystem exchange into assimilation and ecosystem respiration: review and improved algorithm. *Global Change Biology* **11**, 1424–1439 (2005).
109. Lundberg, S. M. & Lee, S.-I. A Unified Approach to Interpreting Model Predictions. in *Advances in Neural Information Processing Systems* vol. 30 (Curran Associates, Inc., 2017).